ELSEVIER

Chemical Geology 163 (2000) 235–245

CHEMICAL GEOLOGY
INCLUDING
ISOTOPE GEOSCIENCE

www.elsevier.com/locate/chemgeo

Meta-gabbro weathering in the Georgia Piedmont, USA: implications for global silicate weathering rates

Paul A. Schroeder [a,*], Nathan D. Melear [a], Larry T. West [b], Dixie A. Hamilton [b]

[a] *Department of Geology, University of Georgia, Athens, GA 30602-2501 USA*
[b] *Crop and Soil Science, University of Georgia, Athens, GA 30602-7272 USA*

Received 16 June 1998; accepted 10 May 1999

Abstract

The mineral assemblages in a vertical weathering profile developed over a meta-gabbro terrain were studied for their stoichiometry and relative abundances. The site is located in the Piedmont Province in the southeast portion of the Appalachians orogenic belt in a forested residual landscape and a temperate climate. The soil is classified as a fine mixed thermic Ultic Hapludalf and defined by distinct A-, B- and C-horizons with thicknesses of 17, 62 and ~250 cm, respectively. The primary mineral assemblage consists of 44% (wt.%) andesine, 40% hornblende, 6% quartz, 4% biotite, 3% ilmenite/titanomagntite/rutile/sphene grains and 3% epidote. Quantitative XRD, detailed XRD clay mineralogy and thin-section petrography revealed the incipient breakdown of the primary minerals to vermiculite (after biotite oxidation), randomly ordered mixed-layer mica/vermiculite/smectite (as grain coatings), kaolin group minerals (after mafic silicate dissolution), goethite and hematite. Vermiculite (after biotite), expandable clay coatings and all the primary minerals (with exception to quartz) are dissolved away from the A-horizon. Hydroxy-interlayered-vermiculite and minor amounts of gibbsite occur as tertiary phases in the A-horizon. Using mineral stoichiometries and average abundances for the parent rock and C-, B- and A-horizon, estimates of primary mineral mass loss were determined. The bicarbonate to silica ratio expected from the mineral loss reactions is 6 times higher than the ratio observed in average groundwater of the Georgia Piedmont. This suggests that, although weathering of mafic terrains is important to the long-term process of transferring CO_2 to the oceans, the present day contribution of silicate weathering in temperate climates may be more largely influenced by the weathering of felsic terrain.

Keywords: Meta-gabbro; Weathering; Georgia Piedmont, USA

1. Introduction

There is little doubt that silicate weathering of continental crust is an essential process in stabilizing the long-term global geochemical cycles of elements such as carbon in the atmosphere (Berner and Berner, 1987). CO_2 is removed from the atmosphere via hydrolysis reactions between carbonic acid and silicates. The weathering of mafic silicates is particularly important because the soluble ions of Ca^{2+}, Mg^{2+} and HCO_3^- formed during weathering, are

* Corresponding author. Tel.: +1-706-542-2384; fax: +1-706-542-2425; E-mail: schroe@gly.uga.edu

0009-2541/00/$ - see front matter
PII: S0009-2541(99)00129-1

ultimately sequestered and buried in the oceans as carbonate minerals. At the same time, felsic silicates also undergo weathering and deliver soluble K^+, Na^+ and HCO_3^- to the oceans. The dissolution and precipitation rates at which the mineral constituents of felsic versus mafic silicate terrain undergo during weathering are still being established (Velbel, 1992; Velbel et al., 1996). The extent to which silicate weathering is responsible for contributing to the consumption of CO_2 via weathering has therefore yet to be firmly established.

In this light, geochemical mass balance studies of mafic and felsic terrains are an essential starting point for revealing the importance of silicate weathering. Mass balance approaches must start with an accurate characterization of the parent, secondary and tertiary mineral assemblages present in the weathering profile. Most present day mineral assemblages in a weathering profile represent a dynamic balance between the addition of parent rock through regional uplift and the removal processes of physical and chemical mass loss (Pavich, 1989). The types and quantities of minerals however, can also be considered to represent a snapshot of relict steady-state conditions that may have formed in response to different regional climatic conditions. The purpose of this study is to assess the mineral assemblages associated with a temperate upland weathering profile whose parent rock-type is mafic in composition. This study is intended to provide a contextual backdrop for future comparative mass-balance studies to be used to reconcile the importance of mafic versus felsic weathering to the balance of the carbon cycle.

1.1. Study site

The study site lies within the Woodville Quadrangle, in the Daniel Springs community, Greene County, GA, USA (82°75′42″ longitude, 33°39′00″ latitude). The region comprises part of the Paleozoic Piedmont Province to the southeast of the Appalachians Mountains. The study site has affinities to the Carolina Slate Belt which contains abundant volcanoclastic rocks intruded by mafic to felsic dikes that have been subsequently metamorphosed (Lovingood, 1983; Conway, 1986). The specific coring site is located in a large (15 km^2) area that has been mapped as the Daniel Springs meta-gabbro. The site occurs on a local topographic high (elevation 165 m) and aside from potential aeolian inputs, it is assumed to be a wholly residual weathering profile.

It is likely that the land was once cultivated (50 years ago) for agricultural use and it is assumed that soils were not tilled beyond 30 cm depth. Present day vegetation consists of mature mixed deciduous and coniferous forest. Mean annual rainfall is 125 cm $year^{-1}$ and mean annual temperature is 23°C (Hodler and Schretter, 1986).

2. Methods

Sampling was performed with both a hand auger and a Gidding's® hydraulic coring device mounted on a truck. The core stem utilized a 5-cm diameter core tube. The soil profile was described using standard terminology (Soil Survey Staff, 1993). Munsell colors and Hurst's color index (H^*L/C) were determined on moist samples.

Both whole rock/saprolite/soil material and size-fractionated materials were examined for mineral content. The clay-size fraction (<2 μm) was separated using wet sieving and centrifugation techniques (Hathaway, 1956). Major mineral modal analysis and clay mineralogical analysis were performed using X-ray powder diffraction (XRD). XRD analyses were conducted using a Scintag XDS-2000 diffractometer. Experimental parameters were optimized for quantification (Hurst et al., 1997) and included CuKα radiation, 40 kV, 35 mA, 1°/2° divergence slits, 0.5°/0.3° receiving slits and a scan rate of 2°2θ/min. Quantitative XRD measurements were made using reference-intensity-ratios derived from a 20% by weight added α-Al_2O_3 internal standard (Chung, 1974a,b). Peaks for the various minerals were referenced to the internal standard peak (α-Al_2O_3) at 43.3°2θ.

Clay samples were sedimented to infinite thickness on glass petrographic slides and air-dried (Moore and Reynolds, 1997). The clays were pretreated with K^+ and Ca^{2+} saturation and then analyzed in the air-dried, ethylene glycol, 300°C and 550°C treated states for identification of hydroxy-interlayered vermiculite (HIV), gibbsite, kaolinite and mixed-layer

mica/smectite. Kaolinite and halloysite were not discriminated in the quantitative XRD results therefore, all 7.1 Å phases represented in the diffractograms are hereafter collectively referred to as kaolin group minerals.

Mixed-layering XRD patterns were simulated using NEWMOD® (Reynolds, 1985). Trioctahedral smectite and trioctahedral mica structures were used as input for layer types. The upper limit of scattering domain size (N) was set to 6, so as to approximately reproduce the peak broadening seen in the observed diffraction patterns.

A petrographic microscope and electron microprobe were employed to examine detailed grain morphological relationships and for mineral identification. Thin sections were prepared using standard vacuum epoxy impregnation methods (Fitzpatrick, 1993). Sections were polished and selected grains were chemically analyzed using an electron microprobe (JEOL superprobe®) operating at 15 kV and 15 nA.

3. Results

3.1. Soil description

The coring operation retrieved 200 cm of continuous sampling. A schematic description of the soil/saprolite profile is shown in Fig. 1. The soil is classified as a fine, mixed, thermic Ultic Hapludalf and displays properties similar to the regional Macklenburg and Enon Series mapped in nearby Oglethorpe County (Frost, 1991). In general terms, the depth profile of recovered core contains a 0–17 cm A-horizon, a 17–79 cm B-horizon and a 79–200 cm portion of the C-horizon. Coring and auguring

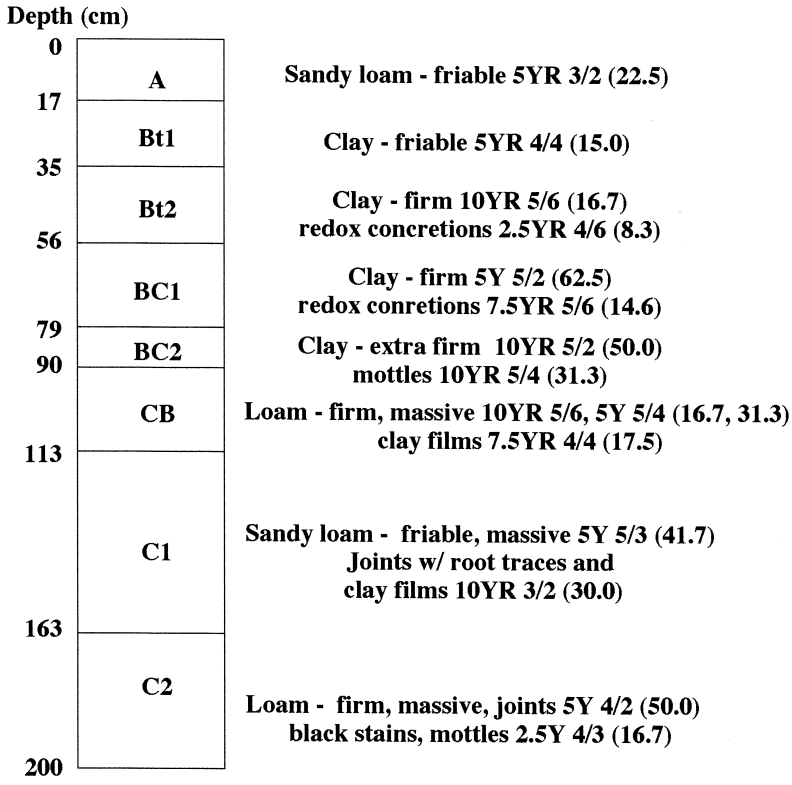

Fig. 1. Detailed soil description of the core taken from Daniel Springs, GA. Colors are based on the Munsell system and by the iron content color index (H^*L/C) of Hurst (1977).

resistance encountered at 200 cm suggests that parent rock occurs within 300 cm of the surface.

3.2. Parent rock mineralogy

Quantitative analysis of the underlying Daniel Springs meta-gabbro can be inferred from petrographic examination of the saprolite (Fig. 2a) in conjunction with previous petrographic studies. Lovingood (1983) conducted a thorough modal analysis of the Daniel Springs meta-gabbro using samples from within the mapped area. Modal analysis however, only provides mineral abundance data on a volume basis. In order to compare the petrographic observations of Lovingood (1983) to quantitative XRD results of this study (reported on a weight percent basis), modal abundances were recast using the average specific gravity for each primary phase present (Deer et al., 1992). Using this approach (less accessory phases), the meta-gabbro has recalculated

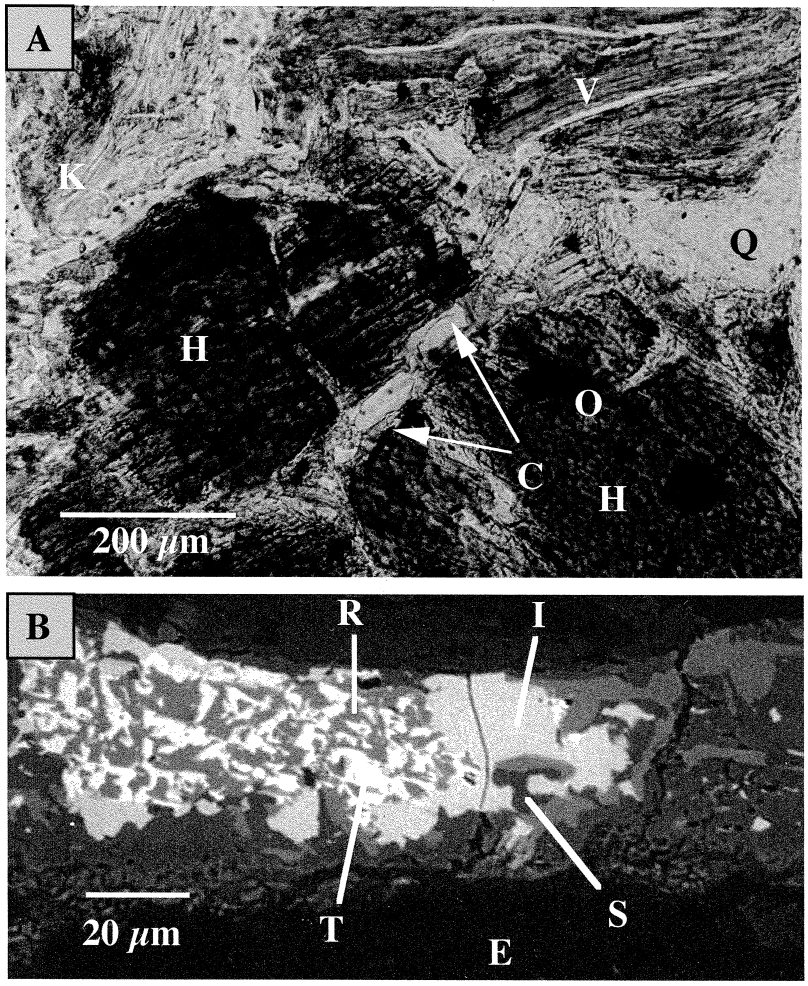

Fig. 2. (a) Thin section photograph of saprolite taken from a depth of 124 cm below the surface. H = hornblende, K = kaolinite, V = vermiculite after biotite, C = pore lining expandable clay, Q = quartz, O = opaque Fe–Ti-bearing phase 'ilmentite'. (b) Backscatter electron image of the opaque Fe–Ti-bearing grains. In decreasing order of brightness: I = ilmenite, T = titanomagnetite, R = rutile, S = sphene and E = epoxy resin.

Table 1
Weight percent oxide analysis of mineral grains from Daniel Springs meta-gabbro saprolite at 170 cm depth

Oxide	Plagioclase	Amphibole	Epidote	Mica
SiO_2	57.95	42.98	37.51	38.68
Al_2O_3	26.66	12.56	23.58	15.34
TiO_2	0.00	0.16	0.13	1.48
Fe_2O_3[a]	0.00	0.00	12.80	9.66
FeO[a]	0.00	15.60	0.00	5.36
MnO	0.00	0.32	0.23	0.09
MgO	0.00	10.30	0.02	11.71
CaO	8.54	11.69	22.83	1.19
Na_2O	6.49	1.54	0.00	0.45
K_2O	0.03	0.33	0.02	3.53
Totals[b]	99.67	95.48	97.12	87.49

[a]Fe was measured as total Fe. The following assignments were made based on published analysis of similar species for which oxidation states were determined (Deer et al., 1992). Fe in the amphibole was assumed ferrous. Fe in epidote was assumed ferric. Fe in vermiculite was proportioned 2/3 ferric and 1/3 ferrous.
[b]Oxides are not reported on a water-free basis.

mineral abundances of: plagioclase (An_{40}), 44%, hornblende 40%, epidote 3%, quartz 6%, biotite 4% and ilmenite/titanomagnetite/titantite/rutile/sphene 3%. The latter Fe- and Ti-bearing phases are most commonly found together, occurring as exsolved species in single opaque grains (Fig. 2b). For the purposes of this study, these opaque grains are collectively referred to as ''ilmenite'' and represented by the average composition $(FeO)_{0.40}(Fe_2O_3)_{0.40}(TiO_2)_{0.20}$.

Petrographic observation of the saprolite and microprobe analysis of residual primary plagioclase and amphibole agrees well with the above estimates (see below and Table 1). Using the oxide data in Table 1, the data have been recast into structural formulae for the plagioclase, epidote and amphibole. Their formulae are $Na_{0.58}Ca_{0.42}Al_{1.42}Si_{2.58}O_8$ (andesine), $Ca_{1.96}Fe^{3+}_{0.77}Al_{2.23}Si_{3.00}O_{12}(OH)$ and $Na_{0.45}Ca_{1.90}Mg_{2.33}Fe^{2+}_{1.98}Al_{0.80}Si_{6.53}Al_{1.45}Ti_{0.02}O_{22}(OH)_2$ (hornblende), respectively. Unaltered biotite grains were not observed in the thin section. Therefore, biotite compositions were estimated on basis of microprobe analyses performed on biotites found in surrounding rocks. Using the published microprobe analysis of biotite by Schroeder et al. (1997) and several performed as part of petrology class projects at the University of Georgia, an average composition of $K_{0.86}Mg_{1.21}Ti_{0.09}Fe^{2+}_{1.25}Al_{0.40}Si_{3.00}Al_{1.00}O_{10}(OH)_2$ is assumed.

3.3. C-horizon mineralogy

Fig. 3 shows representative clay mineral XRD patterns from within the profile. The deepest clay mineral assemblage in the weathering profile contains both kaolin group minerals and expandable 2:1 clays. Results from modeling of mixed-layer XRD patterns using NEWMOD indicate the presence of both smectitic and vermiculite layer types with a high-charged heterogeneous layer charge distribution. This is supported by the comparative response of Ca- and K-saturated samples (Fig. 3). Ca-saturated samples display characteristics of a mixed-layer 10 Å/17 Å, with 90% expandable layers and random ordering (reichweite or $R = 0$). The same sample displays 10 Å/17 Å mixed-layering, with 50% ex-

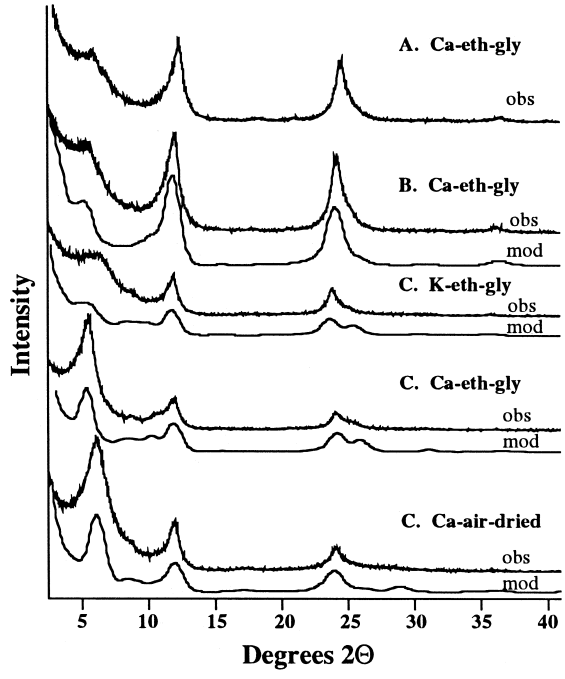

Fig. 3. Observed and modeled X-ray powder diffraction patterns of < 2 μm fraction from samples representative of the A-, B- and C-horizons. obs = observed data, mod = modeled data, Ca- = calcium saturated, K- = potassium saturated, eth-gly = ethylene glycol saturated, air-dried = relative humidity ~50%. °2θ units based on CuKα radiation.

pandable layers and $R = 0$ ordering when K-saturated. The difference in expandability between the Ca- and K-saturated samples indicates that roughly half of the smectite layer types are high-charged (i.e., > 0.5 interlayer equivalent per half unit formula).

Based on the X-ray pattern in Fig. 3, the expandable clays, vermiculite and mixed-layer illite/smectite appear to be the dominant clay present in the C-horizon, however, this is not the case. A relative comparison of the calculated diffraction pattern intensities for the mixed-layer illite/smectite and kaolinite, indicate that the kaolin group minerals are quantitatively the dominant clay, even though the (001) kaolin group reflections appear with lower intensity. Study of Fe-substitution in kaolinites by Schroeder and Pruett (1996) and Schroeder et al. (1998) have shown that most kaolins display near ideal stoichiometry relative to other clays. The upper limit of ferric Fe-substitution for Al in kaolinite is about 1 in 30 (i.e., $Al_{1.93}Fe_{0.07}Si_2O_5(OH)_4$). Considering the contribution of Fe of kaolin minerals is small relative to other Fe-bearing minerals, their composition is idealized to be $Al_2Si_2O_5(OH)_4$ for the purposes of this study.

Petrographic examination of C-horizon saprolite supports the XRD observations that clays are both expandable and kaolin group minerals. In thin section, kaolin minerals predominantly occur as replacements to the framework minerals, plagioclase, hornblende, epidote and mica (Fig. 2a). Vermiculite occurs from the alteration of pre-existing 2:1 biotite. Recasting of the oxide data (Table 1) into a 2:1 structural formula, results in a vermiculite that typically results from the alteration of biotite (Schroeder et al., 1997; Murphy et al., 1998). Assuming two-thirds of the ferrous iron is oxidized to the ferric state, the vermiculite half-unit formula is $K_{0.35}Mg_{1.21}Ti_{0.09}Fe^{3+}_{0.58}Fe^{2+}_{0.25}Al_{0.40}Si_{3.00}Al_{1.00}O_{10}(OH)_2$. The smectitic clays appear as authigenic pore linings or grain coatings on the skeletal frameworks grains (labeled as C in Fig. 2a). The light olive coloration (5Y 5/3) of the saprolite matrix is suggestive of a ferroginous smectite. Translocated clay textures were not observed in C-horizon.

Incipient alteration of the Ti- and Fe- bearing ''ilmenite'' phases is apparent in thin section and by coloration. Clay films bearing 10YR 3/2 coloration are indicative of goethite (Hurst, 1977). Bulk XRD data also indicate the presence of minor amounts of goethite. Melear and Schroeder (1999) have documented that incipient goethite formed within the C-horizon of Piedmont weathering profiles typically contain 10% Al substitution for Fe (on a molar basis) in the structure. The goethite in the C-horizon can probably be represented by the formula $Al_{0.1}Fe_{0.9}OOH$.

3.4. B-horizon mineralogy

This clay-rich horizon is dominated by the kaolin group minerals. Fig. 3 shows this in the X-ray pattern of the clay fraction, which has small amounts of mixed-layer mica/vermiculite/smectite. XRD analysis of the bulk material reveals the disappearance of the framework silicates plagioclase, hornblende, mica and epidote, as well as ilmenite towards the top of the B horizon. Small redox concretions with reddish 2.5YR 4/6 coloration indicate fine (~ 1.0 μm) hematite is present (Schwertmann and Cornell, 1991). Bulk XRD data also indicate the presence of minor amounts of goethite and hematite. The amount of quartz, relative to the C-horizon is significantly greater.

3.5. A-horizon mineralogy

The upper-most horizon features a predominance of quartz, kaolin group minerals and hydroxy-interlayered-vermiculite. Only a minor amount of gibbsite was detected in the clay fraction. The HIV is distinctly different from the expandable mixed-layer clays found deeper in the profile. Fig. 3 shows HIV's signature 14 Å reflection. The unheated sample's peak position does not respond to changes in cation-, hydration- or ethylene glycol-solvation state. Coloration (5YR 3/2) indicates fine hematite, goethite and organic matter are present (Hurst, 1977). Bulk XRD data also indicate the presence of minor amounts of goethite and hematite. Melear and Schroeder (1999) have documented that incipient goethite formed within the A-horizon of the Piedmont weathering profiles can contain 30% Al substitution for Fe (on a molar basis) in the structure. The goethite formed in the A-horizon can probably be represented by the formula $Al_{0.3}Fe_{0.7}OOH$.

4. Discussion

4.1. Mineral reactions

Changes in the mineral assemblage observed in the Daniel Springs meta-gabbro weathering profile are graphically summarized in Fig. 4. Quantitative analysis clearly show the chemical breakdown of the primary minerals andesine, hornblende, biotite, epidote and ilmenite. The accumulation of secondary minerals, kaolin group, vermiculite, mixed-layer mica/smectite, hematite and low-Al-goethite at the expense of the primary minerals is also apparent. The minerals HIV and high-Al-goethite are formed at the expense of secondary minerals and are characteristic of near-surface weathering profile throughout the Piedmont (Melear and Schroeder, 1999). Residual amounts of quartz increase (five-fold the parent rock amount) towards the surface to the point where it is a dominant primary mineral constituent in the A- and B-horizons. The fact that gibbsite occurs in only trace amounts in the Daniel Springs A-horizon, suggests that advective transport factors are less important than those in A-horizons located on near-by felsic terrains. This is supported by the observations that gibbsite commonly in occurs A-horizon of felsic weathering profiles in the Piedmont (Melear and Schroeder, 1999) and in mafic terrains of the mountainous southern Blue Ridge (Velbel, 1989).

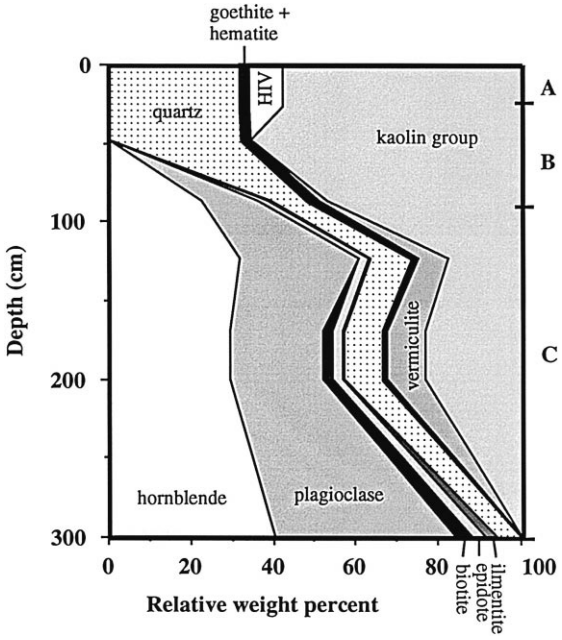

Fig. 4. Normalized relative weight percent abundances of the major and minor phases in Daniel Springs meta-gabbro weathering profile estimated using XRD and thin section petrography.

Table 2 contains the major mineral species observed within the weathering profile, along with their stoichiometries and relative abundances. The average molar abundances of the elements for each horizon have been calculated using the data from Table 2 to examine for net elemental gains and losses (Table 3). Whole-rock/soil elemental analysis unfortunately, were not available at the time of this study and the inaccuracies inherent in XRD quantification ($\pm 5\%$ of the reported values) allow only an assessment of elements that show large differences.

Table 3 shows that relative to the parent rock, large net losses of Mg, Ca and K have occurred across each successively higher horizon. Relative to the parent rock, Al, H and O show net enrichments in the C-horizon and B-horizon, while they show a small net loss in the A-horizon relative to the B-horizon. Si abundance shows no real systematic changes between horizons. The Fe and Ti values in Table 2 are likely subject to quantification errors and without bulk elemental analysis, any interpretation would be suspect. It is clear however, that even with rough estimates of the relative oxidation state of Fe in each phase, the abundance of ferric iron relative to ferrous iron increases upward in the profile. Using the observations in Tables 2 and 3 we propose a series of simple weathering reactions occurring within each horizon. These weathering reactions below are similar to those proposed by Velbel (1989; 1992) and by Murphy et al. (1998).

4.1.1. Reactions involving primary phases

(1) Plagioclase (andesine) dissolution → kaolin group: $Na_{0.58}Ca_{0.42}Al_{1.42}Si_{2.58}O_8 + 4.45H_2O + 1.42CO_2 \rightarrow 0.42Ca^{2+} + 0.58Na^{+} + 1.16H_4SiO_4^{\circ} + 0.71Al_2Si_2O_5(OH)_4 + 1.42HCO_3^{-}$.

(2) Hornblende dissolution → kaolin group + low Al-goethite + anatase: $Na_{0.45}Ca_{1.90}Mg_{2.33}Fe^{2+}_{1.98}Al_{0.80}Si_{6.53}Al_{1.45}Ti_{0.02}O_{22}(OH)_2 + 17.94H_2O + 10.89CO_2 + 0.50O_2 \rightarrow 1.90Ca^{2+} + 0.45Na^{+} + 2.33Mg^{2+} + 2.18Al_{0.1}Fe_{0.9}O(OH) +$

Table 2
Mineral stoichiometries and abundances (weight fraction) in the Daniel Springs weathering profile. Abundances given below are normalized to unity and constrained by XRD, thin section petrography and coloration

Mineral	Formula	A-horizon (0–17 cm)	B-horizon (17–90 cm)	C-horizon (90–300 cm)	Parent rock (> 300 cm)
Plagioclase	$Na_{0.58}Ca_{0.42}Al_{1.42}Si_{2.58}O_8$	0.000	0.068	0.258	0.440
Hornblende	$Na_{0.45}Ca_{1.90}Mg_{2.33}Fe^{2+}_{1.98}Al_{0.80}Si_{6.53}Al_{1.45}Ti_{0.02}O_{22}(OH)_2$	0.000	0.115	0.307	0.400
Epidote	$Ca_{1.96}Fe^{3+}_{0.77}Al_{2.23}Si_{3.00}O_{12}(OH)$	0.000	0.013	0.024	0.030
Biotite[a]	$K_{0.86}Mg_{1.21}Ti_{0.09}Fe^{2+}_{1.25}Al_{0.40}Si_{3.00}Al_{1.00}O_{10}(OH)_2$	0.000	0.000	0.013	0.040
Quartz	$Si\,O_2$	0.317	0.207	0.095	0.060
Ilmenite	$(FeO)_{0.40}(Fe_2O_3)_{0.40}(TiO_2)_{0.20}$	0.000	0.003	0.004	0.030
Vermiculite	$K_{0.35}Mg_{1.21}Ti_{0.09}Fe^{3+}_{0.31}Fe^{2+}_{0.63}Al_{0.40}Si_{3.00}Al_{1.00}O_{10}(OH)_2$	0.000	0.010	0.083	0.000
Kaolin	$Al_2Si_2O_5(OH)_4$	0.579	0.567	0.207	0.000
Goethite — low-Al[b]	$Al_{0.1}Fe_{0.9}O(OH)$	0.010	0.007	0.001	0.000
Goethite — high-Al[b]	$Al_{0.3}Fe_{0.7}O(OH)$	0.005	0.003	0.000	0.000
Hematite	Fe_2O_3	0.012	0.009	0.009	0.000
HIV[c]	$Ca_{0.08}K_{0.24}Mg_{0.20}Fe^{3+}_{0.24}Al_{2.21}Si_{3.23}O_{15.79}H_{5.79}$	0.078	0.000	0.000	0.000
Anatase[d]	$Fe_{0.05}Ti_{0.95}O_2(OH)_{0.05}$	0.004	0.001	0.000	0.000

[a]Composition modified from Schroeder et al. (1997).
[b]Composition from Melear and Schroeder (1999).
[c]Composition from Kirkland and Hajek (1972).
[d]Composition from Shiflet (1999).

$4.48H_4SiO_4^\circ + 1.02Al_2Si_2O_5(OH)_4 + 0.02Fe_{0.05}Ti_{0.95}O_2(OH)_{0.05} + 10.89HCO_3^-$.

(3) Biotite redox-transformation (biotite composition adapted from Schroeder et al., 1997) → vermiculite + low-Al-goethite: $K_{0.86}Mg_{1.21}Ti_{0.09}Fe^{2+}_{1.25}Al_{0.40}Si_{3.00}Al_{1.00}O_{10}(OH)_2 + 1.01CO_2 + 1.11H_2O + 0.10\ Ca^{+2} + 0.50O_2 + 0.09H_4SiO_4^\circ \rightarrow Ca_{0.10}K_{0.35}Mg_{1.21}Ti_{0.09}Fe^{3+}_{058}Fe^{2+}_{0.25}\ Al_{0.40}Si_{3.09}Al_{0.96}\text{-}O_{10}(OH)_2 + 0.51K^+ + 0.46\ Al_{0.1}Fe_{0.9}O(OH) + 1.01HCO_3^-$.

Table 3
Elemental abundance (mmol/g) in the Daniel Springs meta-gabbro and weathering horizons based on mineral stoichiometries and abundances

Element	A	B	C	Parent
Si	9.75	9.66	9.43	9.82
Ti	0.00	0.01	0.03	0.06
Al	4.48	5.10	4.06	3.43
Fe^{2+}	0.00	0.28	0.85	1.09
Fe^{3+}	0.31	0.27	0.24	0.24
Mg	0.00	0.33	1.07	1.15
Ca	0.00	0.40	1.13	1.62
Na	0.00	0.19	0.67	1.08
K	0.00	0.01	0.09	0.08
H	9.13	9.21	4.39	1.14
O	31.26	32.69	29.32	27.45

(4) Biotite redox-dissolution → kaolinite + low-Al-goethite: $K_{0.86}Mg_{1.21}Ti_{0.09}Fe^{2+}_{1.25}Al_{0.40}Si_{3.00}Al_{1.00}O_{10}(OH)_2 + 7.81H_2O + 4.53CO_2 + 0.31O_2 \rightarrow 0.63Al_2Si_2O_5(OH)_4 + 0.86K^+ + 1.21Mg^{2+} + 1.39Al_{0.1}Fe_{0.9}O(OH) + 1.74H_4SiO4^\circ + 0.09Fe_{0.05}Ti_{0.9}O_2(OH)_{0.05} + 4.53HCO_3^-$.

(5) Epidote dissolution → kaolin group + low-Al-goethite: $Ca_{1.96}Fe^{3+}_{0.77}Al_{2.23}Si_{3.00}O_{12}(OH) + 5.70H_2O + 3.92CO_2 \rightarrow 1.96Ca^{2+} + 0.86Al_{0.1}Fe_{0.9}O(OH) + 0.86H_4SiO_4^\circ + 1.07Al_2Si_2O_5(OH)_4 + 3.92HCO_3^-$.

(6) Quartz dissolution: $SiO_2 + H_2O \rightarrow H_4SiO_4^\circ$

(7) Ilmenite redox → hematite and anatase: $(FeO)_{0.40}(Fe_2O_3)_{0.40}(TiO_2)_{0.20} + 0.10O_2 \rightarrow 0.60Fe_2O_3 + 0.21Fe_{0.05}Ti_{0.95}O_2(OH)_{0.05}$.

4.1.2. Reactions involving tertiary phases

(8) Vermiculite redox-dissolution → kaolin group + high-Al goethite + anatase: $Ca_{0.10}K_{0.35}Mg_{1.21}Ti_{0.09}\,Fe^{3+}_{058}\,Fe^{2+}_{0.25}\,Al_{0.40}Si_{3.09}Al_{0.96}O_{10}(OH)_2\ 6.58H_2O + 3.22CO_2 + 0.06O_2 \rightarrow 0.10Ca^{2+} + 0.35K^+\ 1.21Mg^{2+} + 1.19Al_{0.3}Fe_{0.9}O(OH) + 2.09H_4SiO_4^\circ\text{-} + 0.50Al_2Si_2O_5(OH)_4 + 0.09\ Fe_{0.05}Ti_{0.95}O_2\text{-}(OH)_{0.05} + 3.22HCO_3^-$.

(9) Vermiculite redox-transformation + kaolinite → HIV (composition idealized after Kirkland and Hajek, 1972) + high-Al goethite: $Ca_{0.10}\ K_{0.35}$-

$Mg_{1.21}Ti_{0.09}Fe^{3+}_{058}Fe^{2+}_{0.25}Al_{0.40}Si_{3.09}Al_{0.96}O_{10}(OH)_2 + 3.12H_2O + 1.92CO_2 + 0.12O_2 + 0.55Al_2Si_2O_5(OH)_4 \rightarrow 0.02Ca^{2+} + 0.11K^+ + 1.01Mg^{2+} + Ca_{0.08}K_{0.24}Mg_{0.20}Fe^{3+}_{0.24}Al_{2.21}Si_{3.23}O_{15.79}H_{5.79} + 0.85Al_{0.3}Fe_{0.7}O(OH) + 0.96\ H_4SiO_4^\circ + 0.09Fe_{0.05}Ti_{0.95}O_2(OH)_{0.05} + 1.92HCO_3^-$.

(10) Kaolin group + low-Al goethite dissolution → high-Al goethite: $0.09\ Al_2\ Si_2O_5(OH)_4 + Al_{0.1}Fe_{0.7}O(OH) + 0.27H_2O \rightarrow Al_{0.3}Fe_{0.7}O(OH) + 0.18H_4SiO_4^\circ$.

4.2. Reaction fronts at horizons

The well-defined horizons in this study allow for a simplified system that is subdivided into four regions, defined by the parent rock, C-horizon, B-Horizon and A-horizon. Each subdivision is characterized by the stoichiometry and abundance of the minerals. Petrographic observations and the relative mass loss and gain/enrichment of each mineral constituent in each horizon therefore define the dominant mineral reactions occurring between adjacent horizons. For example, the mineral assemblage of the parent meta-gabbro is related to those in the C-horizon by the sum of reactions 1, 2, 3, 4, 5 and 7 given above. The overall reaction, therefore constitutes the incipient weathering front, as it moves into the parent rock, which in this case, involves (a) the dissolution of plagioclase, hornblende, epidote, biotite and ilmenite, (b) the transformation of biotite to vermiculite and (c) the precipitation of kaolin group minerals, hematite, low-Al goethite and vermiculite. Soluble reaction products presumably undergo downward/lateral advective removal from each horizon. In the case of clays with exchangeable cation sites, temporary fixing of divalent species (i.e., Ca^{2+}) relative to monovalent species via interlayer cation exchange is likely to be favored. This is supported by the chemical analysis of the vermiculite after biotite (Table 1). A portion of soluble ions such as K^+ are also known to be retained and cycled in the A- and B-horizons by plant root metabolic uptake and subsequent release by the bacterial decay of leaves returned to the forest floor.

Using the stoichiometric and quantitative data from Tables 2 and 4 was generated by recasting the mineral abundance data to an atomic basis (i.e., mmol/g of mineral reactant or product). Included in Table 4 are the net differences for each solid phase in the parent, C- and B-horizons relative to their overlying horizon. In the cases where a negative difference is observed, then a minimum material loss has been assumed. No assumptions therefore, have been made in this study about using a conservative component (e.g., Ti used by Brimhall and Dietrich, 1987). Positive values of non-preexisting phases represent new mineral growth. Positive values of preexisting phases could reflect either a concentration of residual quantities and/or additional precipitated mineral mass. Using the molar values in Table 4, overall reactions occurring between adjacent horizons are proposed below. The overall reactions between each set of horizon pairs are constrained by dissolution of all phases (excluding quartz) in the underlying horizon using stoichiometries dictated in reactions 1–10. Aqueous species are presumed to be laterally transported away from each horizon.

Table 4
Estimated mineral molar abundances in the parent (P) Daniel Springs meta-gabbro, C, B and A weathering horizons and changes in molar abundance across horizons (negative values indicate millimoles lost). Units are millimoles per gram of solid. dashes (–) indicate the mineral is absent

Mineral[a]	A	B	C	P	A/B	B/C	C/P
Plagioclase	–	0.235	0.888	1.515	−0.24	−0.65	−0.63
Hornblende	–	0.128	0.344	0.449	−0.13	−0.22	−0.10
Biotite	–	–	0.029	0.088	0.00	−0.03	−0.06
Epidote	–	0.028	0.054	0.068	−0.03	−0.03	−0.01
Quartz	5.267	3.448	1.587	0.999	1.82	1.86	0.59
Ilmenite	–	0.027	0.029	0.241	−0.03	0.00	−0.21
Vermiculite	–	0.022	0.190	–	−0.02	−0.17	0.19
Kaolin	2.241	2.192	0.802	–	0.05	1.39	0.80
Anatase	0.004	0.005	0.006	–	0.00	0.00	0.00
Goethite	0.167	0.11	0.005	–	0.06	0.10	0.00
Hematite	0.073	0.056	0.058	–	0.02	0.00	0.06
HIV	0.167	–	–	–	0.17	0.00	0.00

[a] See Table 2 for stoichiometries.

The net reaction between the parent and the C-horizon can be generalized as follows: 63 Plagioclase + 10 hornblende + 6 biotite + 1 epidote + 21 ilmenite + 486 $H_2O + 213CO_2 + 9O_2 \rightarrow 5$ vermiculite + 59 kaolin + 26 low-Al-goethite + 13 hematite + 4 anatase + $25Mg^{2+} + 47Ca^{2+} + 41Na^+ + 3K^+ + 120H_4SiO_4^\circ + 213HCO_3^-$.

The net reaction between the C-horizon and the B-horizon can be generalized as follows: 65 Plagio-

clase + 22 hornblende + 3 biotite + 3 epidote + 16 vermiculite + 789H_2O + 396CO_2 + 13O_2 → 75 kaolin + 53 low-Al-goethite + 2 anatase + 71Mg^{2+} + 75Ca^{2+} + 48Na^+ + 6K^+ + 183$H_4SiO_4°$ + 396 HCO_3^-.

The net reaction between the B-horizon and the A-horizon can be generalized as follows: 24 Plagioclase + 13 hornblende + 3 epidote + 3 Ilmenite + 2 vermiculite + 362H_2O + 190CO_2 + 7O_2 → 1 HIV + 34 kaolin + 31 high-Al-goethite + 1 low-Al-goethite + 2 hematite + 1 anatase + 33Mg^{2+} + 41Ca^{2+} + 20Na^+ + 1K^+ + 89$H_4SiO_4°$ + 190HCO_3^-.

The weathering reactions proposed above indicate that distinctly different geochemical environments occur within the profile. This is exemplified by the changes in the secondary mineral assemblage and the ratios of cations generated. It is likely the differences are due to infiltration rate and reactive surface areas (Berner and Berner, 1987). Reactive mineral surface area of mafic silicates in the C-horizon are related to etch pit formation (seen in thin section) and to expandable clay coatings (Fig. 3). The net effect of the clay coating would be to inhibit dissolution. In the B-horizon, expandable clay coats are disrupted by compaction and bioturbation mechanisms and lost via dissolution. This then allows for the remaining mafic silicates to dissolve.

On a molar basis, all the reactions shown above release significant bicarbonate and silica. The molar ratio of bicarbonate to silica that would be released from the net reactions in the entire weathering profile has a constant value of about 2. This ratio is notably 6 times higher than the average composition of groundwater for the Georgia Piedmont (Railsback et al., 1996). This suggests that although mafic terrains are potentially significant contributors of bicarbonate to the groundwater system, their role may not be volumetrically commensurate to more deeply weathered and more extensive felsic terrains. A comparison of this mafic mineral assemblage to a nearby, more felsic weathering profile would help in this analysis. The preponderance of quartz in the A- and B-horizons and release of dissolved silica would further suggest that there is not significant quartz dissolution in the C and B horizons, and perhaps in the special case of poorly-drained mafic terrains in the Piedmont, quartz abundance could serve a conservative tracer.

5. Conclusions

Mineralogical results of a weathering profile developed over a meta-gabbro reveal the primary minerals plagioclase, hornblende, epidote, biotite, quartz and ilmenite are present in the saprolite. The minerals plagioclase, hornblende and epidote are etched and possess clay coatings. Secondary phases in the saprolite include: randomly-ordered mixed-layer mica/vermiculite/smectite (90% expandable layer-type with Ca-saturation, 60% expandable with K-saturation), kaolinite, goethite and vermiculite (after biotite). Plagioclase, amphibole, vermiculite and ilmenite systematically decrease from the C to the B horizon. Kaolinite dominates the B horizon clay mineralogy. The near surface, A horizon, assemblage is characterized by the presence of hydroxy-interlayered-vermiculite, kaolinite and abundant quartz.

Based on the stoichiometry and abundance of the minerals observed from the bottom to the top of the weathering profile, relative mineral stabilities occur in the sequence: plagioclase < biotite < hornblende < ilmenite < epidote < mixed-layer mica/vermiculite/smectite < vermiculite < low-Al goethite < kaolin minerals < quartz < hematite < high-Al goethite < HIV. The relative production of bicarbonate to silica, based on mass loss estimates in the mineral assemblage, is six times higher than the bicarbonate to silica ratio regionally observed in groundwater of the Georgia Piedmont. A proposed parallel study from a nearby, equivalent landscape, whose parent material is felsic in composition, in addition to a more detailed aerial estimate of mafic and felsic terrains should provide a basis for comparing the relative rates of felsic silicate weathering versus mafic silicate weathering in temperate climates.

Acknowledgements

This work was supported by a grant to the senior author from the National Science Foundation (EAR9628035). Special thanks go to the junior author's (DAH) clay mineralogy class colleagues, who helped collect the core and provided XRD sample preparation. The editorial review by Mike Velbel significantly improved the manuscript. Dr. Sandra

Wyld kindly allowed the use of her petrographic microscope. Mr. Chris Fleisher facilitated the microprobe analyses. Dr. Mike Roden's petrologic insight was invaluable. [*JD*]

References

Berner, E.K., Berner, R.A., 1987. The global water cycle: Geochemistry and Environment. Prentice-Hall, Englewood Cliffs, NJ, 397 pp.

Brimhall, G.H., Dietrich, W.E., 1987. Constitutive mass balance relations between chemical composition, volume, density, porosity and strain in metasomatic hydrothermal systems: results on weathering and pedogensis. Geochimica et Cosmochimica Acta 51, 567–587.

Chung, F.H., 1974a. Quantitative interpretation of X-ray diffraction patterns of mixtures: I. Matrix-flushing method for quantitative multicomponent analysis. Journal of Applied Crystallography 7, 519–526.

Chung, F.H., 1974b. Quantitative interpretation of X-ray diffraction patterns of mixtures: II. Adiabatic principle of X-ray diffraction analysis of mixtures. Journal of Applied Crystallography 7, 526–531.

Conway, K.M., 1986. The Geology of The Northern Two-Thirds Of The Philomath Quadrangle, GA. Geology Department, University of Georgia, Athens, GA, p. 137.

Deer, W.A., Howie, R.A., Zussman, J., 1992. An Introduction to the Rock-forming Minerals. Longman Group, Hong Kong, 696 pp.

Fitzpatrick, E.A., 1993. Soil Microscopy And Micromorphology. Wiley, New York, USA, 304 pp.

Frost, L.W., 1991. Soil Survey of Oglethorpe County, GA. US Department of Agriculture, Soil Conservation Service, Washington, DC.

Hathaway, J.C., 1956. Procedure for clay mineral analysis used in the sedimentary petrology laboratory of the US Geological Survey. Clay Minerals Bulletin 3, 8–13.

Hodler, T.W., Schretter, H.A., 1986. The Atlas of Georgia. Institute of Community Area Development, The University of Georgia, Athens, GA, 273 pp.

Hurst, V.J., 1977. Visual estimation of iron in saprolite. Geological Society of America Bulletin 88, 174–176.

Hurst, V.J., Schroeder, P.A., Styron, R.W., 1997. Accurate quantification of quartz and other phases by powder X-ray diffractometry. Analytica Chimica Acta 337, 233–252.

Kirkland, D.L., Hajek, B.F., 1972. Formula derivation of Al-interlayered vermiculite in selected soil clays. Soil Science 114 (4), 317–322.

Lovingood, D., 1983. The Geology Of The Southern One-Third Of The Philomath And Northern One-Third Of The Crawfordville, Georgia Quadrangles. Geology Department, University of Georgia, Athens, GA, p. 243.

Melear, N.D., Schroeder, P.A., 1999. Crystal Chemistry of goethites from selected weathering profiles of the Georgia Piedmont: evidence for multigenerational mineral assemblages. Geoderma, in review.

Moore, D.E., Reynolds, R.C., 1997. X-ray diffraction and the identification and analysis of clay minerals, 2nd edn. Oxford Univ. Press, Oxford, 378 pp.

Murphy, S.F., Brantley, S.L., Blum, A.E., White, A.F., Dong, H., 1998. Chemical weathering in a tropical watershed, Luquillo Mountains, Puerto Rico: II. Rate and mechanism of biotite weathering. Geochimica et Cosmochimica Acta 62 (2), 227–243.

Pavich, M.J., 1989. Regolith residence time and the concept of surface age of the Piedmont ''peneplain''. Geomorphology 2, 181–196.

Railsback, L.B., Bouker, P.A., Feeney, T.P., Goddard, E.A., Goggin, K.E., Hall, A.S., Jackson, B.P., Mclain, A.A., Orsega, M.C., Rafter, M.A., Webster, J.W., 1996. A survey of the major-element geochemistry of the Georgia groundwater. Southeastern Geology 36 (3), 99–122.

Reynolds, R.C., 1985. NEWMOD — A Computer Program for the Calculation of One-dimensional Diffraction Patterns of Mixed-layered Clays. R.C. Reynolds, 8 Brook Rd., Hanover, NH 03755.

Schroeder, P.A., Pruett, R., 1996. Iron ordering in kaolinites: insights from ^{29}Si and ^{27}Al NMR spectroscopy. American Mineralogist 81, 26–38.

Schroeder, P.A., Kim, J.G., Melear, N.D., 1997. Mineralogical and textural criteria for recognizing remnant Cenozoic deposits on the Piedmont: evidence from Sparta and Greene County, Georgia, USA. Sedimentary Geology 108, 195–206.

Schroeder, P.A., Pruett, R.J., Hurst, V.J., 1998. Effects of secondary iron phases on kaolinite ^{27}*Al* MAS NMR spectra. Clays and Clay Minerals 46, 429–435.

Schwertmann, U., Cornell, R.M., 1991. Iron Oxides in the Laboratory: Preparation and characterization. VCH, Weinheim, Germany, 137 pp.

Shiflet, J.A., 1999. Characterization of titanium bearing phases in an east Georgia Kaolin. MS Thesis, University of Georgia, Athens, GA. 100 pp.

Soil Survey Staff, 1993. Soil Survey Manual. US Department of Agriculture Handbook 18. US Government Printing office, Washington, DC, 437 pp.

Velbel, M.A., 1989. Weathering of hornblende to ferruginous products by a dissolution-precipitation mechanism: petrography and stoichiometry. Clays and Clay Minerals 37 (6), 515–524.

Velbel, M.A., 1992. Geochemical mass balances and weathering rates in forested watersheds of the southern Blue Ridge: III. Cation budgets and the weathering rate of amphibole. American Journal of Science 292, 58–78.

Velbel, M.A., Charles, L., Basso, J., Zieg, M.J., 1996. The natural weathering of staurolite: crystal-surface textures, relative stability, and the rate-determining step. American Journal of Science 296, 453–472.